



Porosity model and pore evolution of transitional shales: an example from the Southern North China Basin

Xiao-Guang Yang^{1,2} · Shao-Bin Guo^{1,2}

Received: 2 March 2020
© The Author(s) 2020

Abstract

The evolution of shale reservoirs is mainly related to two functions: mechanical compaction controlled by ground stress and chemical compaction controlled by thermal effect. Thermal simulation experiments were conducted to simulate the chemical compaction of marine-continental transitional shale, and X-ray diffraction (XRD), CO₂ adsorption, N₂ adsorption and high-pressure mercury injection (MIP) were then used to characterize shale diagenesis and porosity. Moreover, simulations of mechanical compaction adhering to mathematical models were performed, and a shale compaction model was proposed considering clay content and kaolinite proportions. The advantage of this model is that the change in shale compressibility, which is caused by the transformation of clay minerals during thermal evolution, may be considered. The combination of the thermal simulation and compaction model may depict the interactions between chemical and mechanical compaction. Such interactions may then express the pore evolution of shale in actual conditions of formation. Accordingly, the obtained results demonstrated that shales having low kaolinite possess higher porosity at the same burial depth and clay mineral content, proving that other clay minerals such as illite–smectite mixed layers (I/S) and illite are conducive to the development of pores. Shales possessing a high clay mineral content have a higher porosity in shallow layers (<3500 m) and a lower porosity in deep layers (>3500 m). Both the amount and location of the increase in porosity differ at different geothermal gradients. High geothermal gradients favor the preservation of high porosity in shale at an appropriate R_o . The pore evolution of the marine-continental transitional shale is divided into five stages. Stage 2 possesses an R_o of 1.0%–1.6% and has high porosity along with a high specific surface area. Stage 3 has an R_o of 1.6%–2.0% and contains a higher porosity with a low specific surface area. Finally, Stage 4 has an R_o of 2.0%–2.9% with a low porosity and high specific surface area.

Keywords Thermal simulation · Porosity model · Pore evolution · Transitional shale · Southern North China Basin · Shanxi formation

1 Introduction

Shale oil and gas have proven to be a type of unconventional oil and gas resource with abundant reserves (Curtis 2002; Jarvie et al. 2007; Zhang et al. 2018). In the past decade, there have been many successful examples of shale oil and

gas exploration, such as the Barnett Shale in the Fort Worth Basin (Bernard et al. 2012), the Horn River Group shale in the Western Canada Sedimentary Basin (Ross and Bustin 2009; Dong et al. 2015), the Posidonia Shale in Europe (Gasparik et al. 2014), the Devonian Woodford Shale in Oklahoma and Texas, and the Longmaxi Formation in the Sichuan Basin (Tian et al. 2013; Yang et al. 2016). These examples are marine shales rich in Type I and II kerogen, while marine-continental transitional shales rich in Type III kerogen have not yet been found for large-scale commercial exploitation. However, due to its high brittleness, its thin layers arranged into thick cumulative layers and its potential for micro-crack development the marine-continental transitional shale has its own unique advantage of oil and gas exploitation (Luo et al. 2018; Sun et al. 2019).

Edited by Jie Hao

✉ Shao-Bin Guo
guosb58@cugb.edu.cn

¹ School of Energy Resources, China University of Geosciences (Beijing), Beijing 100083, China

² Key Laboratory of Marine Reservoir Evolution and Hydrocarbon Enrichment Mechanism, Ministry of Education, Beijing 100083, China

For shale oil and gas, the shale reservoirs are the most important factors to study. Due to the inherent in situ advantages of shale oil and gas accumulation, the quality of the reservoir space (including pore distribution, pore structure, wettability and connectivity) directly affects the oil and gas accumulation and exploitation. However, this evaluation is currently an incomplete approach based on the current conditions seen because the preservation conditions and historical relationship between the source and reservoir largely determine whether hydrocarbons can be efficiently accumulated (Han et al. 2017).

Regardless of the type of oil and gas research being conducted, the evolution process is an important and difficult topic. Thermal simulation experiments are often used to simulate thermal evolution in the laboratory to discuss hydrocarbon generation and diagenesis of shales (Xie et al. 2014; Akande et al. 2015; Guo and Mao 2019). The thermal maturation process undoubtedly has an important influence on the pore evolution of shale. With the generation of hydrocarbons, many micropores will be generated inside the organic matter, and the micropores will provide a large specific surface area (Modica and Lapierre 2012; Milliken et al. 2013). Organic acids formed during the early maturity of organic matter can dissolve feldspar minerals and form considerable dissolution pores (Baruch et al. 2015). Oil and asphalt fillings can block pores in “oil windows” (Mastalerz et al. 2013). During the high maturity stage, a large amount of kaolinite and chlorite are transformed into illite, and the intermediate product is the illite–smectite mixed layer, which will reform the pore structure and connectivity (Wang and Guo 2019).

However, the rock undergoes more than thermal process during the burial process. As the depth increases, the rock skeleton will experience higher effective stress (Marcusen et al. 2009). Mineral particles slip in the shallow layer, deform in the middle layer, and appear pressure solution in the deep layer. Mechanical compaction has been accompanied by the entire process of diagenesis and not just in the shallow layers (Ramdhan and Neil 2011). Only the fluid pressure can be detected in thermal simulation experiments, yet neither the effective stress nor the pressure on the shale skeleton is not considered. For example, the average porosity of high-mature shale with a burial depth of more than 2500 m is 3.02% in Sichuan Basin (Zou et al. 2010) and 2.8% in Southern North China Basin (Yang and Guo 2020). However, the shale porosity in the thermal simulation experiment is always not less than 4% (Chen and Xiao 2014; Xie et al. 2014; Guo and Mao 2019). Therefore, thermal simulation experiments alone cannot truly reflect the evolution of shale reservoirs. For the pore size characterization of the thermal simulation experiment, compaction correction is required. The difficulty of this problem is that the thermal process and compaction process are not two independent

processes. The thermal process is accompanied by changes in the mineral composition, which lead to the changes in the physical properties of shales and then affect the compaction law of shales.

In this paper, based on thermal simulation experiments of marine-continental transitional shale samples (R_o from 0.96% to 3.38%), characterizing the diagenesis and pore characteristics of the shale via N_2 adsorption, CO_2 adsorption, MIP, X-ray diffraction and SEM. A new compaction formula considering clay content and the proportion of kaolinite was established, and a porosity evolution model that considers chemical compaction and mechanical compaction was proposed. Finally, the pore evolution of marine-continental transitional shale is analyzed under a single burial process and special geothermal conditions.

2 Geological setting

Sedimentary strata can be roughly classified into marine facies, continental facies, and marine-continental transitional facies according to their genesis. In the North China area, Sichuan and Guizhou Provinces, a set of marine-continental transitional facies strata were widely deposited in the Late Paleozoic Permian (Fig. 1b). Organic-rich shale and coal are widely abundant in this formation, which has a considerable potential area for shale oil and gas exploration in China.

The sample was taken from the Southern North China Basin (Fig. 1a, c), which is a Mesozoic and Cenozoic superimposed basin developed on the North China platform (Chen et al. 2016). Affected by global sea level rise in the Late Carboniferous, this area corresponds to epicontinental sea sedimentation. Affected by the uplift of the Yinshan palaeocontinent in the early Permian, the seawater in this area gradually receded, and the Southern North China Basin evolved from marine sediments to continental sediments (Lan et al. 1988; Yu et al. 2018). Therefore, a set of marine-continental transitional coal-bearing strata developed in the Permian Taiyuan and Shanxi Formations (Fig. 1c).

3 Thermal simulation experiment

Thermal simulation is an important method for studying the evolution of source rocks. Based on system openness, thermal simulation experiment can be divided into three types: closed system, semi-open system and open system. In this paper, a closed system hydrolysis method (Xie et al. 2014; Akande et al. 2015) was used. Distilled water of half the sample's weight was added to the gold tube to supplement the water consumed during the pyrolysis. The sample is divided into 10 subsamples, each of which has a mass of 10 g and is ground to a size of 10–15 mesh. The subsamples

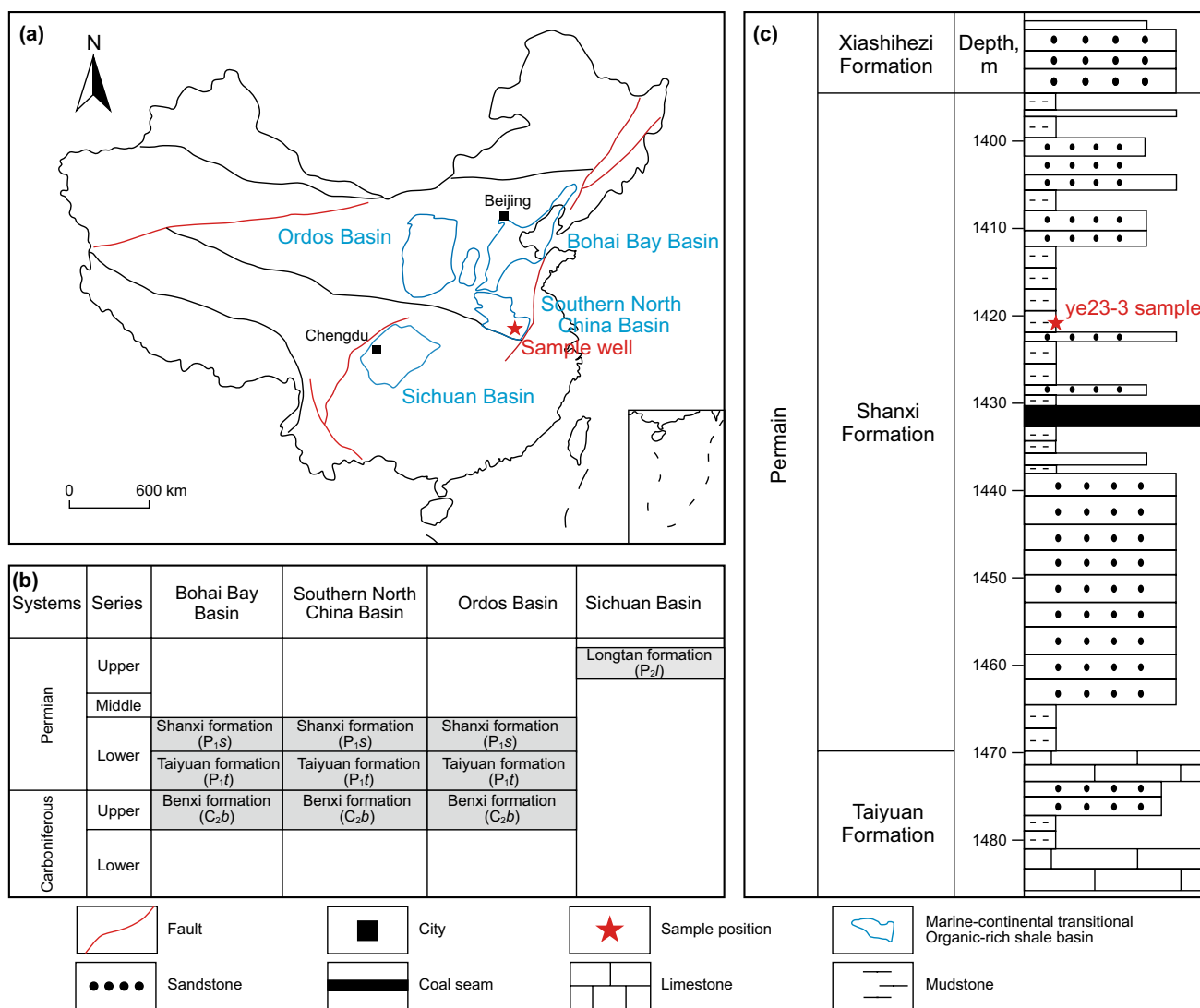


Fig. 1 a Locations of major basins where organic-rich marine-continental transitional shales are developed in China and location of sample well, b formations where organic-rich marine-continental transitional shales are developed and c lithology of sample well and location of ye23-3 sample in the Shanxi Formation

were placed in closed gold tubes filled with argon, and then the gold tubes were placed in a standard autoclave filled with a certain pressure of fluid. The subsamples were heated from 50 °C to 200 °C, 250 °C, 300 °C, 350 °C, 400 °C, 450 °C, 500 °C, 550 °C, 600 °C, and 650 °C in a muffle furnace under a pressure of 50 MPa, and the temperature gradient was 20 °C/h. The temperature error of the autoclave operation was less than 1 °C and the pressure error was less than 1 MPa. After reaching the maximum temperature, the temperature was maintained for 2 h to ensure that the sample was fully pyrolyzed. Finally, the sample was removed from the autoclave and tested separately with X-ray diffraction, CO₂ adsorption, N₂ adsorption, high-pressure mercury injection, and vitrinite reflectance. The basic parameters of the original sample are shown in Table 1.

Table 1 Basic parameters of the ye23-3 sample

Sample ID	Depth, m	R _o , %	TOC, %	Kerogen type
ye23-3	1421.9	0.95	1.55	III

3.1 Diagenesis in thermal evolution

During thermal evolution, the clay minerals in the shale will dehydrate, and then undergo conversion and dissolve, which will cause the pore characteristics of the shale to change. XRD can be used to quantitatively characterize the clay and other rigid mineral contents in shale (Houben et al. 2016). The relative content of the various types of clay minerals is constantly changing with increasing

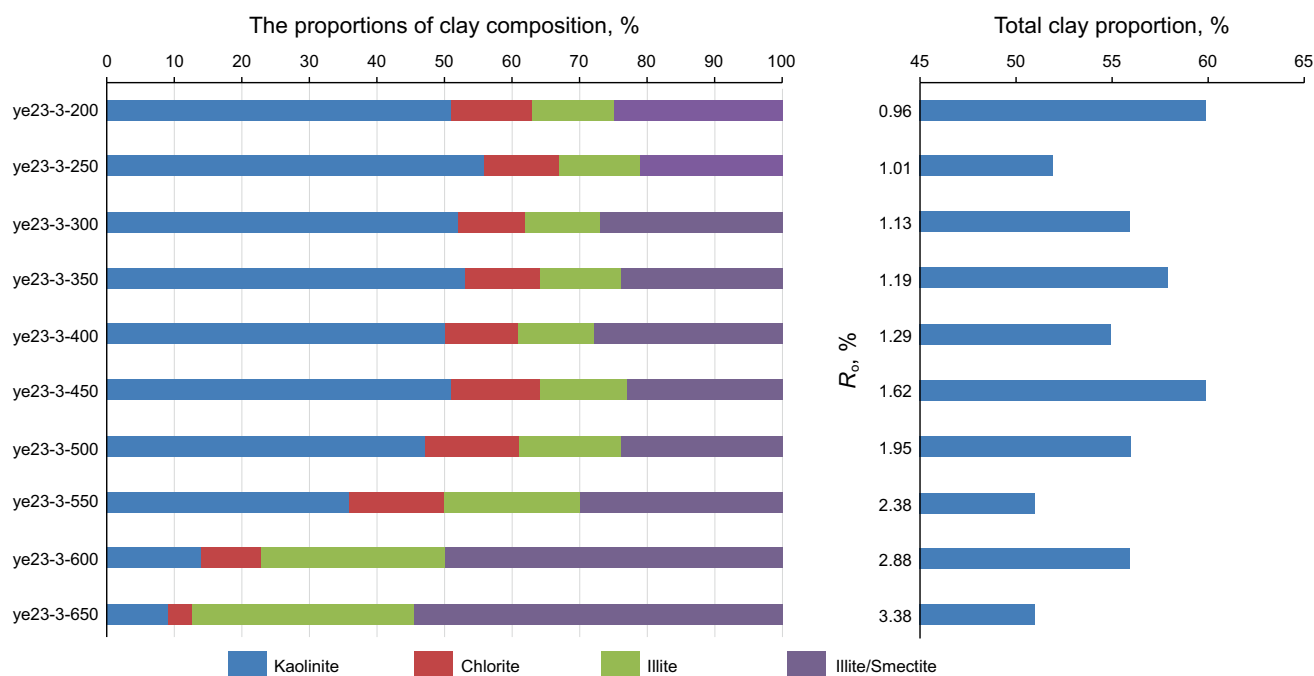


Fig. 2 Proportions of clay mineral compositions and total clay proportion during different degrees of thermal evolution

temperature (Fig. 2). Kaolinite and chlorite decreased with the increase in the degree of thermal evolution, while I/S and illite gradually increased with the degree of thermal evolution. When $R_o < 1.6\%$, the proportions of clay are relatively stable. When $R_o > 1.6\%$, the proportion of kaolinite began to decrease, and the proportions of illite and I/S began to increase. When $R_o = 2.4\%$, with a significant increase in I/S, the conversion speed reaches the maximum while kaolinite decreases rapidly. In addition, the

generation of authigenic quartz leads to a decrease in the total clay proportion (Metwally and Chesnokov 2012). When $R_o = 2.88\%$, the relative content proportions of either kaolinite or chlorite is less than 10%, which infers that both contents are basically consumed. The content of other clay minerals also tended to be stabilized. Eventually, the I/S content was as high as 60%, the illite content was 36%, the chlorite content was 4%, and the kaolinite content was 10% (Table 2). In addition, the total clay proportion also changed during the thermal evolution.

Table 2 R_o and proportions of mineral compositions of the ye23-3 sample

Samples ID	Temperature, °C	R_o , %	The proportions of clay composition, %				The proportions of mineral composition, %				
			K	C	I	I/S	Clay	Quartz	Feldspar	Plagioclase	Siderite
ye23-3-200	200	0.96	51	12	12	25	60	35	1	3	1
ye23-3-250	250	1.01	56	11	12	21	52	43	1	3	1
ye23-3-300	300	1.13	52	10	11	27	56	39	1	3	1
ye23-3-350	350	1.19	53	11	12	24	58	38	1	2	1
ye23-3-400	400	1.29	50	11	11	28	55	40	1	3	1
ye23-3-450	450	1.62	51	13	13	23	60	37	1	2	<1
ye23-3-500	500	1.95	47	14	15	24	56	40	1	3	
ye23-3-550	550	2.38	36	14	20	30	51	46		3	
ye23-3-600	600	2.88	14	9	27	50	56	41		3	
ye23-3-650	650	3.38	10	4	36	60	51	43		6	

K, Kaolinite; C, Chlorite; I, Illite; S, Smectite

3.2 Pore characteristics in thermal evolution

According to the pore size, shale pores are divided into micropores (<2 nm), mesopores (2–50 nm) and macropores (> 50 nm). A large number of micropores and mesopores have been confirmed in shale, and thus, shale pores cannot be fully characterized using MIP (Curtis et al. 2012a; Chen et al. 2016; Liu et al. 2018a, b). We used a combined method of low-temperature CO₂/N₂ adsorption and MIP to characterize the pore size distribution of shale (Table 3). MIP showed the macropore characteristics of shale. The surface area was obtained with the Young-Dupre equation, and the pore volume was obtained with the Washburn equation. N₂ adsorption showed the mesopore characteristics of shale. The surface area was obtained with the Brunauer–Emmett–Teller (BET) equation, and the pore volume was obtained with the Barrett–Joyner–Halenda (BJH) equation. CO₂ adsorption showed the micropore characteristics of shale. The surface area was obtained with the Dubinin–Radshkevich (D–R) equation, and the pore volume was obtained with the Dubinin–Astakhov (D–A) equation.

The total pore volume and specific surface area of the sample both increased, then decreased, and then increased during the thermal simulation (Figs. 3, 4). The largest contribution to the pore volume is macropores, which account for 66%–92%, followed by mesopores, and the lowest contribution to the pore volume is micropores, which are less than 5%. The total pore volume is between 0.0165 and 0.0285 cm³/g, and the total pore volume is the largest when R₀ is 1.13%. The largest contribution to the specific surface area is micropores, which account for 38%–88%, followed by mesopores, which account for 10%–60%, and the lowest contribution to specific surface area is macropores, which account for less than 1%. The total specific surface area is between 2.01 and 6.04 m²/g, and a high specific surface area corresponds to a high pore volume. The mesopore volume reached a minimum value at R₀ = 1.95% and then gradually increased, corresponding to the time of rapid conversion of kaolinite. The macropore volume reached a maximum when R₀ = 1.13%, which may be related to the generation of organic acids and dissolution. The specific surface area of mesopores and micropores reached a minimum when R₀ = 1.6% and then gradually increased. The ratio of the specific surface area of the micropores increases with the increase in the degree of thermal evolution, and the ratio of the specific surface area of the mesopores decreases first and then increases with the degree of thermal evolution.

4 Mechanical compaction model

The changes in shale pores during chemical compaction can be determined through thermal simulation experiments and test methods (CO₂/N₂ adsorption and MIP). During chemical

Table 3 Pore volume and surface area of different pore types in thermal simulation experiment of the ye23-2 sample

Samples ID	Pore volume, cm ³ /g			Pore surface area, m ² /g			The proportions of pore surface area, %							
	The proportions of pore volume, %			Total surface area			The proportions of pore surface area, %							
	Micropore	Mesopore	Macropore	Total pore	Micropore	Mesopore	Macropore	Micropore	Mesopore	Macropore				
ye23-3-200	0.0005	0.005	0.011	0.0165	3.33	30.18	66.49	1.7824	2.7882	0.0102	4.5808	38.91	60.87	0.22
ye23-3-250	0.0009	0.0046	0.0175	0.023	4.05	20	75.96	3.2696	2.3323	0.0075	5.6094	58.29	41.58	0.13
ye23-3-300	0.001	0.005	0.0226	0.0285	3.34	17.47	79.19	3.2234	2.7882	0.0327	6.0443	53.33	46.13	0.54
ye23-3-350	0.0008	0.005	0.0223	0.0281	2.69	17.91	79.4	2.5511	2.4268	0.0118	4.9897	51.13	48.64	0.24
ye23-3-400	0.0007	0.0023	0.0169	0.0199	3.48	11.7	84.82	4.6633	0.8022	0.0113	5.4768	85.15	14.65	0.21
ye23-3-450	0.0005	0.0019	0.0175	0.0199	2.5	9.7	87.8	1.7431	0.5156	0.1146	2.3734	73.45	21.72	4.83
ye23-3-500	0.0005	0.001	0.0193	0.0208	2.45	4.6	92.95	1.7728	0.2193	0.0188	2.0109	88.16	10.91	0.93
ye23-3-550	0.0007	0.0026	0.0137	0.0171	4.37	15.2	80.43	2.5777	0.6633	0.0249	3.2659	78.93	20.31	0.76
ye23-3-600	0.0009	0.0034	0.0161	0.0204	4.47	16.54	78.99	3.1381	0.8479	0.0334	4.0194	78.07	21.1	0.83
ye23-3-650	0.0011	0.0051	0.0191	0.0253	4.23	20.24	75.53	3.7354	1.736	0.0432	5.5146	67.74	31.48	0.78

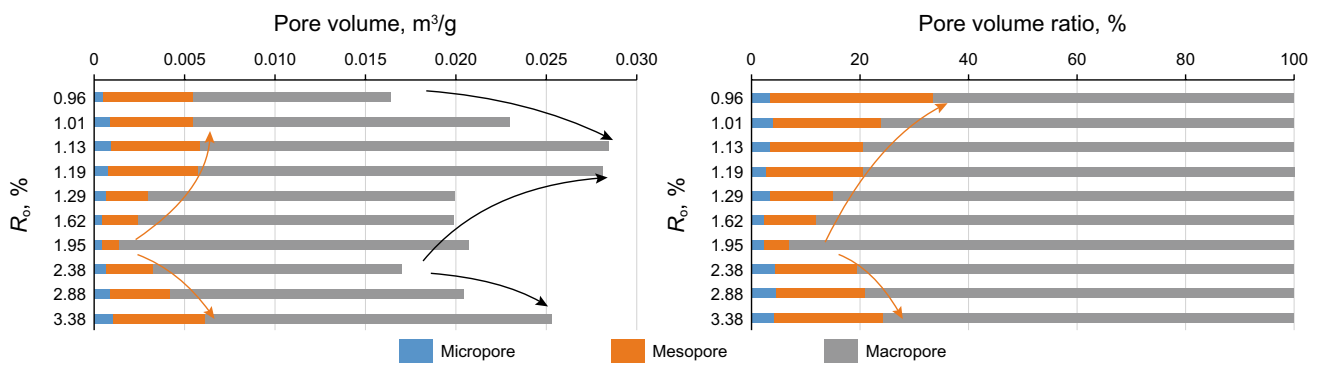


Fig. 3 Pore volumes and proportions of the different pore types

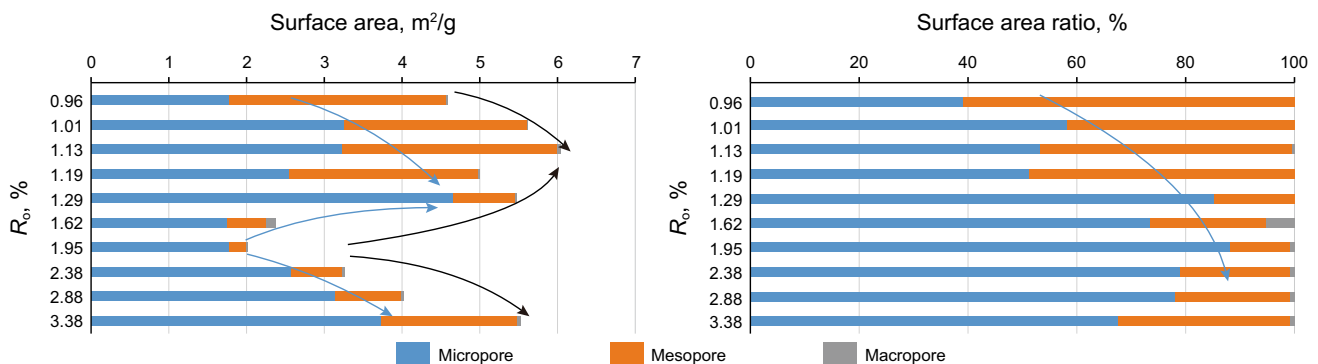


Fig. 4 Pore surface areas and proportions of the different pore types

processes, the changes in pores are mainly controlled by dissolution, cementation and organic matter evolution within shale. Thermal simulation experiments ignore the mechanical compaction of shale because only the fluid pressure is detected and controlled, and the effective stress on the rock skeleton is unchanged during the thermal simulation. However, shale has strong stress sensitivity (Xie et al. 2019), and the influence of the overburden stress on the shale reservoir cannot be ignored. It has been proven that mechanical compaction has a very important pore-reducing effect and thus causes the greatest amount of pore reduction in sediments (White 1986). Mechanical compaction has been increasing with the continuous burial of the formation and has an important impact on the whole diagenesis.

In thermal simulation experiment, the measured pore volume is usually higher which cannot represent the pore evolution of shale under formation conditions. Therefore, the mechanical compaction needs to be taken into consideration in order to correct porosity for its practical significance.

The overburden stress of the rock is shared by the rock skeleton and the fluid in the pores. Effective stress (σ_{eff}) is the stress that the rock skeleton undergoes, and fluid pressure reflects the stress that the fluid undergoes. The effect

of mechanical compaction on the porosity of rocks depends primarily on the effective stress. The higher the effective stress is, the lower the porosity.

The most classic mudstone compaction Eq. was proposed by Athy (1930):

$$\varphi = \varphi_0 * \exp(-K\sigma_{eff}) \tag{1}$$

where φ (%) is the porosity of mudstone; φ_0 (%) is the initial porosity of mudstone; and K is the compaction coefficient.

Bachrach (2017) studied shale compaction experiments and the Gulf of Mexico shale compaction law. He proposed that differences in clay content will affect the physical properties of shale, and high clay content results in stronger compressibility of shale. Equation (1) is changed to:

$$d\varepsilon = d\varphi/\varphi = -K(vcl)d\sigma_{eff} \tag{2}$$

where ε is the strain of shale and vcl is the clay content.

In addition, Gong et al. (2019) produced artificial shales of different clay types and studied the effects of different clay types on its petrophysical properties. The results show that shales with different clay minerals have different petrophysical properties. However, he did not provide a formula

describing the relationship between the effective stress and porosity. The clay mineral content changes significantly during thermal simulation, which will affect the petrophysical properties of shale. Therefore, we divide the content of clay minerals into kaolinite content (ω_k) and other clay mineral content (ω_o) and propose the following Eq. (3):

$$\varphi = \varphi_0 * \exp((-K_1 * \omega_k - K_2 * \omega_o - K_3) * \sigma_{\text{eff}}) \quad (3)$$

where ω_k (%) is the kaolinite content in shale; ω_o (%) is the other clay mineral contents in shale; and K_1 , K_2 and K_3 are the compaction coefficients. For Eq. (3), kaolinite and other clay minerals are considered to have different compaction coefficients (K_1 and K_2 , respectively) to express the differences in petrophysical properties of the different clay minerals. K_3 controls the compaction trend of loose sediments affected by factors unrelated to clay mineral content. When ω_k and ω_o is equal to 0, Eq. (3) is consistent with Eq. (1). Therefore, Eq. (3) with the addition of kaolinite and other clay minerals content can be regarded as a correction of Eq. (1).

When the fluid pressure (P_w) is hydrostatic, the effective stress (σ_{eff}) can be expressed as:

$$\sigma_{\text{eff}}(Z) = (\rho_g - \rho_w) * g * Z \quad (4)$$

where Z (m) is the burial depth; ρ_g (g/cm^3) is the density of rock or shale; and ρ_w (g/cm^3) is the density of formation water.

For the initial porosity (φ_0) of shale, Yin (1992) measured the initial porosity of sand-mud mixed sediments, and the results are shown in Fig. 5. The results show that the sediments mixed with 85% sand and 15% clay have the lowest

initial porosity (34%). When the total clay content higher than 15%, the initial porosity increases as the total clay content increases, and the initial porosity of all clay sediments is as high as 62%. The relationship between the initial porosity and the proportion of clay minerals can be well represented by Eq. (5):

$$\varphi_0 = -0.189 * \omega^2 + 0.567 * \omega + 0.249 \quad (0.15 < \omega < 1) \quad (5)$$

$$\omega = (\omega_k + \omega_o) / 100 \quad (6)$$

where ω is the proportion of total clay in shale.

By substituting Eq. (4) into (3) and taking the natural logarithm on both sides, an equation was determined for the porosity with kaolinite content (ω_k), other clay mineral contents (ω_o) and burial depth (Z):

$$\ln(\varphi/\varphi_0) = -(a * \omega_k + b * \omega_o + c) * Z \quad (7)$$

where a , b and c are the coefficients and φ_0 is calculated by Eqs. (5) and (6).

Equation (7) is an empirical formula for shale porosity loss due to mechanical compaction. We selected the pore volume data of the marine-continental transitional shales of Shanxi Formation in the Southern North China Basin and Longtan Formation in Guizhou Province (from Ma and Guo 2019) to fit the mechanical compaction model. Considering the uniform distribution of data points and data reliability, four wells data with different maximum burial depths were selected. The maximum burial depths of their sampling intervals were 2458–3028 m, 3275–3576 m, 3613–3644 m, and 4284–4332 m. The micropore volume is obtained with

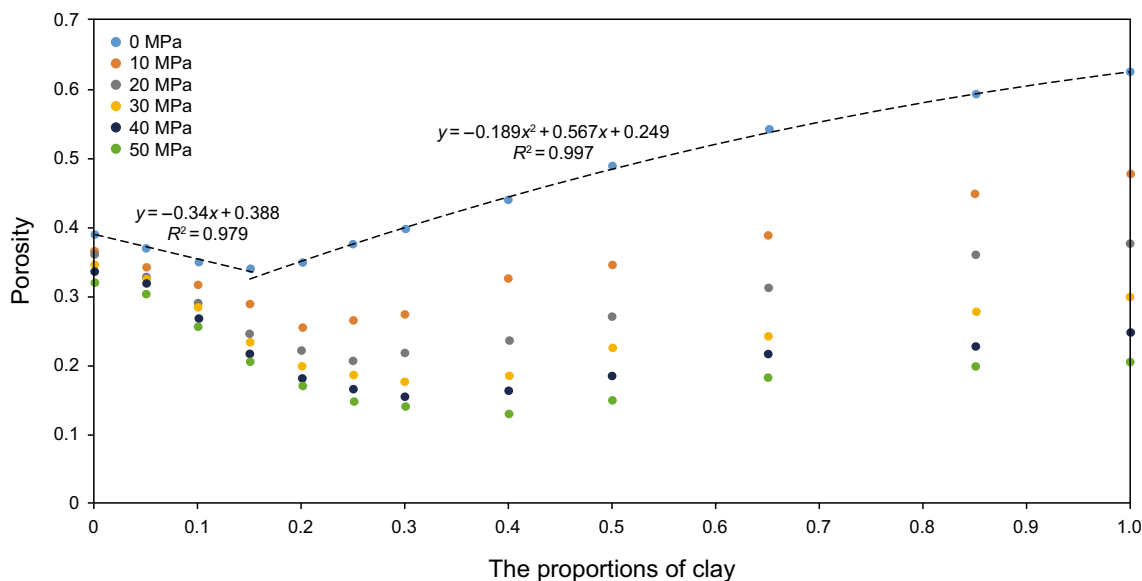


Fig. 5 Relation between the porosity and pressure of sand-mud mixed sediments. Modified by Yin (1992)

CO₂ adsorption, the mesopore volume is obtained with N₂ adsorption, the macropore volume is obtained with MIP, and the clay mineral content is obtained with XRD. The data were derived from the same laboratory, as previously discussed, with the same testing methods and the same testing instruments (Table 4).

Figure 6 shows the relationship between the maximum burial depth and the pore volume. The relationship between micropores and maximum burial depth is disordered, while the volume of mesopores + macropores has a significant exponential relationship with the maximum burial depth. The micropores in shale are mainly organic pores (Yang et al. 2016; Wood and Hazra 2017), which are tiny pores inside the organic matter. Figure 7 shows the characteristics of the pores and organic matter in shale under compaction. The large organic pores are in the same direction as the organic matter, which proves that they are affected by compaction, while the tiny organic pores often remain round and oval. The tiny organic pores often have very high fluid pressure due to hydrocarbon generation, which will prevent the pores from being compacted. In addition, oils and asphaltenes were formed and discharged from the edges of the organic matter to occupy the surrounding pores when the organic matter matured (Fig. 7b, d). This phenomenon can block pores in the early stages of organic matter maturation (Valenza et al. 2013), but in

the high maturation stage, these oils and asphaltenes will degrade and crack again, generating new organic pores and improving reservoir conditions. Therefore, mechanical compaction mainly results in the loss of mesopores and macropores, while the micropore volume is mainly controlled by the content of organic matter and thermal evolution.

The relationship between the porosity of mesopores + macropores (φ_{me+ma}) and the volume of mesopores + macropores (V_{me+ma}) is as follows:

$$\varphi_{me+ma} = \rho_g * V_{me+ma} \tag{8}$$

Using the data in Table 4 to fit Eq. (7), the result is expressed using Eq. (9), and the R² is 0.804.

$$\ln(\varphi_{me+ma}/\varphi_0) = -(0.000296 * \omega_k + 0.000175 * \omega_o + 0.000592) * Z \tag{9}$$

where φ_0 is calculated by Eqs. (5) and (6).

Equation (9) shows that at the same burial depth and the same total clay content, shale with a high proportion of kaolinite has a lower porosity, which proves that kaolinite has a faster loss in porosity than other clay materials (Fig. 8a). Shales with a higher clay mineral content have a higher shallow layer porosity and a faster loss in porosity. After the burial depth exceeds 3500 m, shales with a higher clay content have lower porosity (Fig. 8b).

Table 4 Fitting parameters of the shale porosity of the marine-continental transitional shale (the data of Longtan Formation from Ma and Guo 2019)

Samples ID	Lithology	Formation	Current depth m	Maximum depth m	R _o , %	Pore volume, m ³ /g				ω_k , %	ω_o , %
						Micropore	Mesopore	Macropore	Total pore		
ye23-2	Shale	Shanxi	1413.2	3613.2	0.94	0.0016	0.0101	0.0028	0.0145	46.17	34.83
ye23-5	Shale	Shanxi	1432.6	3632.6	1.05	0.0013	0.0051	0.0122	0.0186	30.16	21.84
ye23-8	Shale	Shanxi	1444.2	3644.2	1.14	0.0019	0.0062	0.0046	0.0126	21.08	40.92
ye31-1	Shale	Shanxi	2684.4	4284.4	3.2	0.0009	0.0050	0.0064	0.0123	12	28
ye31-2	Shale	Shanxi	2732.5	4332.5	3.2	0.0020	0.0051	0.0037	0.0108	11.075	33.225
y1t-1	Shale	Longtan	358.5	2458.5	0.86	0.0033	0.0235	0.0061	0.0329	22.91	56.09
y1t-2	Shale	Longtan	678	2778	1.15	0.0025	0.0269	0.0062	0.0356	14.11	68.89
y1t-3	Shale	Longtan	828.6	2928.6	1.17	0.0028	0.0175	0.0068	0.0271	12.35	52.65
y1t-4	Shale	Longtan	852.6	2952.6	1.06	0.0026	0.0247	0.0045	0.0318	21	54
y1t-5	Shale	Longtan	928.8	3028.8	1.02	0.0028	0.0178	0.0054	0.0261	25.08	40.92
xd-1	Shale	Longtan	1075.5	3275.5	2.5	0.0011	0.0092	0.0076	0.0179	3.6	14.4
xd-2	Shale	Longtan	1175.8	3375.8	2.54	0.0024	0.0088	0.0061	0.0173	0	33
xd-3	Shale	Longtan	1219.6	3419.6	2.56	0.0015	0.0094	0.0099	0.0207	0	32
xd-4	Shale	Longtan	1234.3	3434.3	2.6	0.0022	0.0116	0.0029	0.0167	0	30
xd-5	Shale	Longtan	1328.6	3528.6	2.76	0.0045	0.0131	0.0050	0.0226	0	51
xd-6	Shale	Longtan	1339.5	3539.5	2.8	0.0031	0.0110	0.0048	0.0189	0	33
xd-7	Shale	Longtan	1355.1	3555.1	2.84	0.0036	0.0148	0.0039	0.0223	0	46
xd-8	Shale	Longtan	1376.2	3576.2	2.91	0.0030	0.0094	0.0068	0.0192	0	31

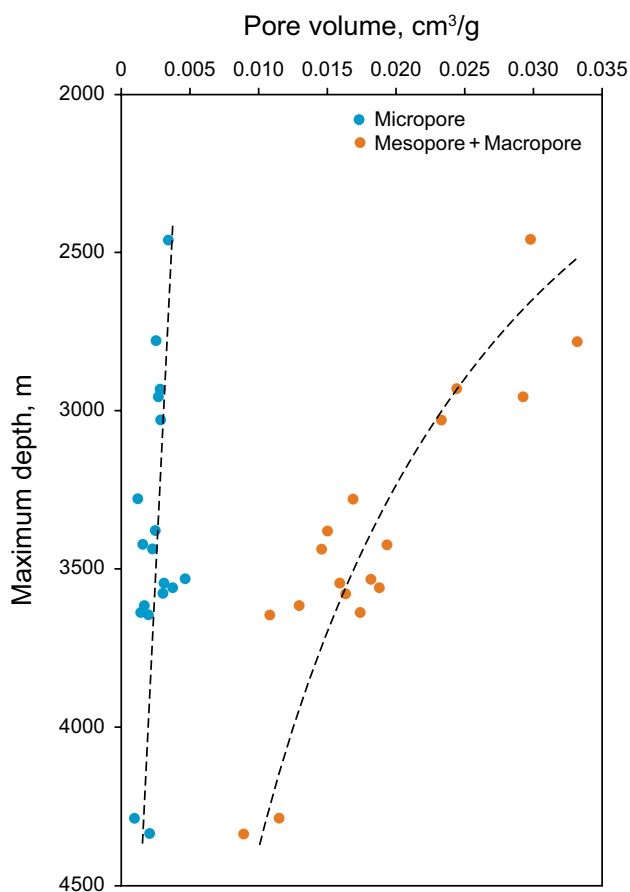


Fig. 6 Relationship between the pore volume and maximum burial depth of the marine-continental transitional shale

5 Discussion

5.1 Porosity model of marine-continental transitional shale

Neither chemical compaction due to thermal processes nor mechanical compaction due to increased effective stress is independent: in the burial of shale, both processes proceed simultaneously. Changes in mineral composition caused by thermal evolution will lead to changes in the physical properties of shales, and the increase in pressure and temperature caused by the burial process will continue the thermal evolution.

The differential form of Eq. (9) can be used to calculate the porosity loss per unit depth of the ye23-3 sample in the thermal simulation experiment:

$$d\varphi_{me+ma}(Z, R_o) = f(\omega_k, \omega_o)dZ \tag{10}$$

Equation (10) combines thermal simulation experiments and mechanical compaction. A computer can use Eq. (10) to

calculate the porosity evolution of the ye23-3 sample under any thermal burial history.

Figure 9a shows the porosity evolution of the ye23-3 sample under different geothermal conditions. The relationship between R_o and temperature is based on Teichmüller (1971). The red dotted line is the porosity evolution path of the thermal simulation experiment, which does not take into account the mechanical compaction caused by increasing burial depth. The red solid line is the porosity evolution path of the ye23-3 sample under actual formation conditions, which takes into account the porosity loss caused by mechanical compaction. The real path is the porosity evolution path when the geothermal gradient is 26 °C/km, which is the average geothermal gradient of the ye23 well. Different geothermal gradients correspond to different porosity evolutions. Figure 9b is a comparison of the porosity evolution considering mechanical compaction and the porosity evolution of thermal simulation experiments only. Without considering the overpressure, when the burial depth is 6000 m (R_o is approximately 2.45), the mesopore and macropore volume of the sample from the thermal simulation experiment is still 4%. This amount is not different from the porosity at a depth of 3000 m, which is obviously unreasonable. In the new pore model, the porosity increased significantly when R_o was in the range of 1.0%–1.2%, and the porosity continued to decrease during the subsequent burial process. However, the rate of porosity loss at different maturity stages is significantly different, which is related to the diagenetic evolution and changes in the pore structure during the thermal evolution.

Higher geothermal gradients are conducive to the preservation of higher porosity at the same R_o , which is a result of less effective stress (Fig. 10a). When R_o is 1%–1.3%, the porosity increases obviously; when R_o is 1.3%–1.9%, the porosity decreases relatively slowly; when R_o is 1.9%–2.3%, the porosity decreases significantly; when R_o is > 2.3%, the porosity decreases slowly again. The porosity increasing stage of shale with higher geothermal gradients appears at a shallower layer and has an increase in higher porosity (Fig. 10b). However, the porosity of the mesopores + macropores of the marine-continental transitional shale constantly vary between the maximum porosity trend and the minimum porosity trend. We speculate that the reason why the porosity is lower than the normal compaction trend is mainly because the thermal evolution increases the clay mineral content; the reason why the porosity is higher than the normal compaction trend is mainly because of the dissolution of organic acids and the conversion of clay minerals to produce interlayer pores. In addition, some clay minerals will be transformed into authigenic quartz to increase the compaction resistance of shale (Metwally and Chesnokov 2012; Liu et al. 2018a, b).

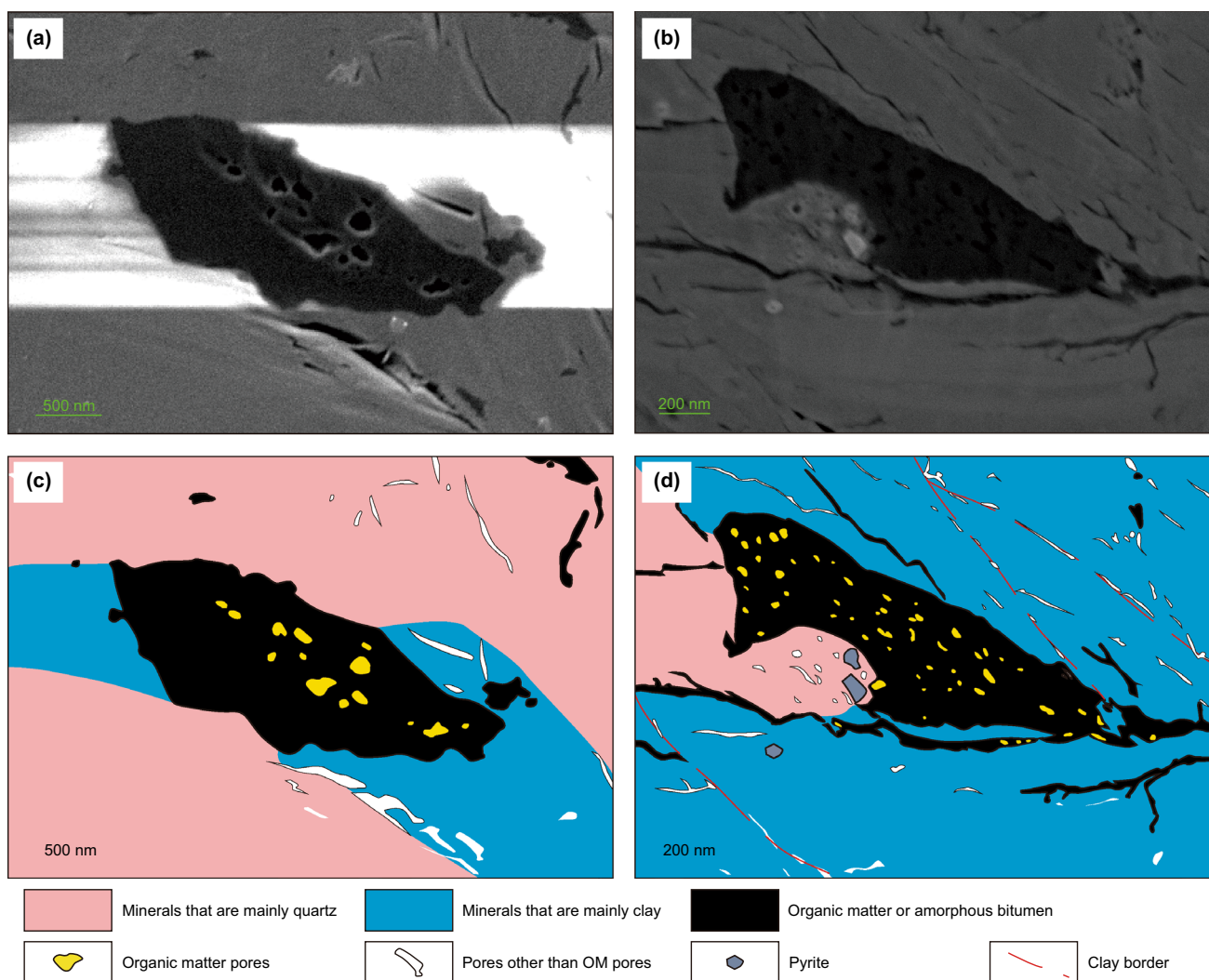


Fig. 7 Organic matter and pore characteristics of the ye23-2 and ye 23-8 samples. **a, c** are scanning electron microscope photographs of argon ion sections and **b, d** are cartoon pictures of the samples

5.2 Pore evolution of marine-continental transitional shale

Combining thermal simulation experiments, diagenetic models, and porosity evolution models, the evolution of marine-continental transitional shale can be divided into five stages under a simple burial process and a specific geothermal gradient (26 °C/km) (Fig. 11). The evolution can be applied to exploration and porosity can be compared with actual shale reservoirs. It is worth pointing out that the overpressure was not considered in the study. The main reason overpressure was not considered is that marine-continental transitional shale is different from marine shale. It has a thin single layer (less than 4 m) and contains silty sand, which makes overpressure difficult to form. In addition, paleo-overpressure is difficult to predict, and finding reliable fluid inclusions in shale is difficult. Moreover, whether it is fluid inclusions

or other means, there is a large error, so overpressure is not considered in this article.

Stage 1, $R_0 \leq 1.0\%$, $T \leq 95$ °C. The most important mechanism affecting reservoirs at Stage 1 is mechanical compaction. As the burial depth increases, the movable water in the pores flows to the shallow layer, and the volume and specific surface area of the mesopores and macropores decrease rapidly. Biomethane and a small amount of low-maturity oil are also generated. As the formation temperature gradually increases, organic matter begins to enter the “oil window” and generates a small amount of oil. The type of organic matter is type III, which produces few organic matter pores at this stage. Therefore, the micropore volume is small enough to be ignored, but the specific surface area of the micropore is gradually increased.

Stage 2, $1.0\% < R_0 \leq 1.6\%$, 95 °C $< T \leq 120$ °C. The kerogen has matured and produced a large amount of organic

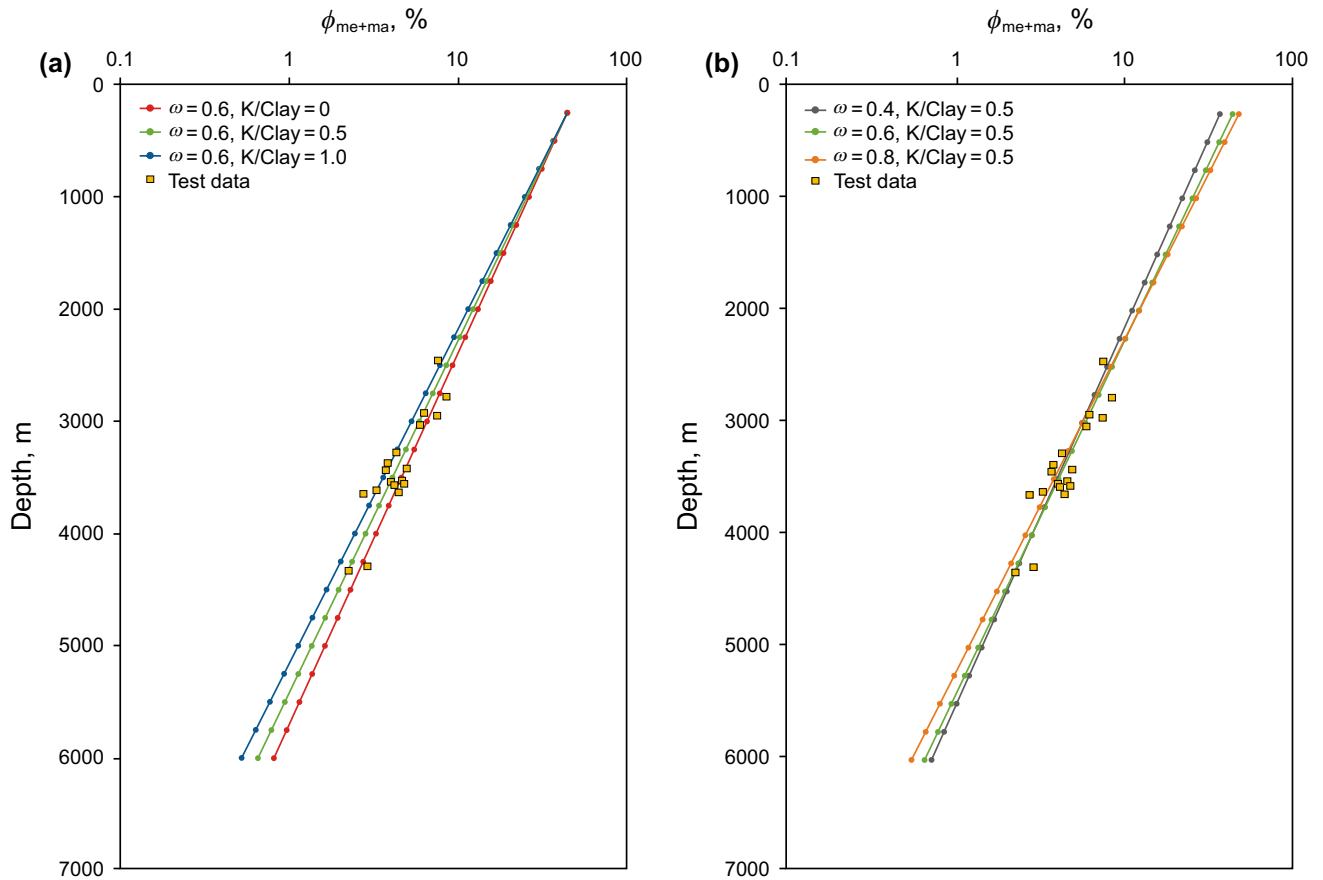


Fig. 8 Loss in porosity loss for the compaction models with different clay contents and kaolinite proportions

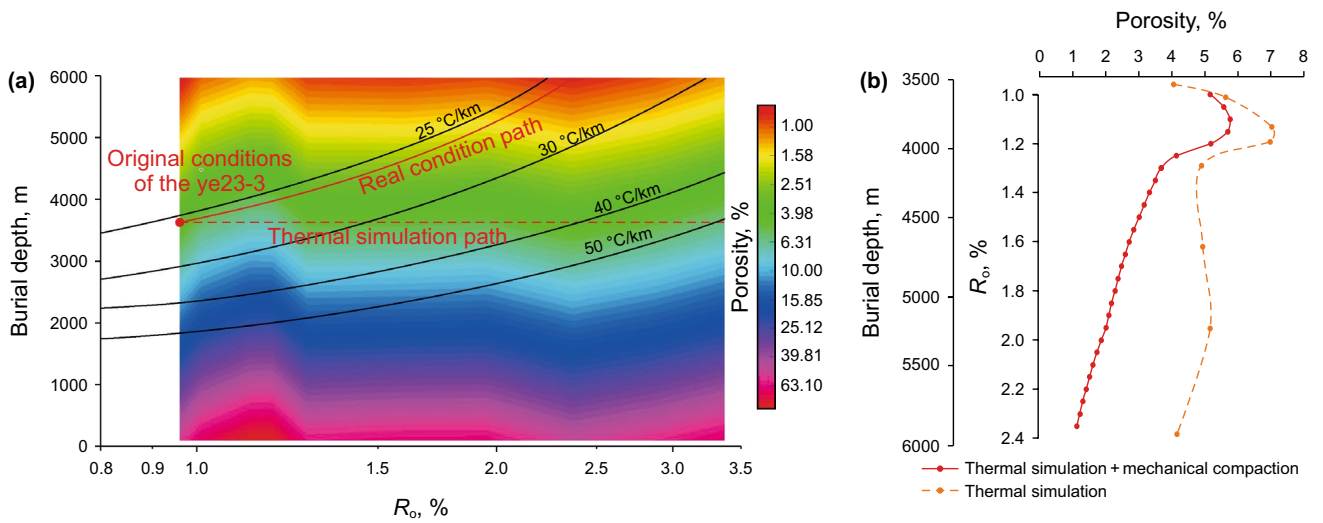


Fig. 9 **a** The porosity changes under different geothermal conditions of the ye23-3 sample, considering both mechanical compaction and thermal simulation. **b** Comparison of the porosity evolution considering mechanical compaction and the porosity evolution of the thermal simulation experiments only

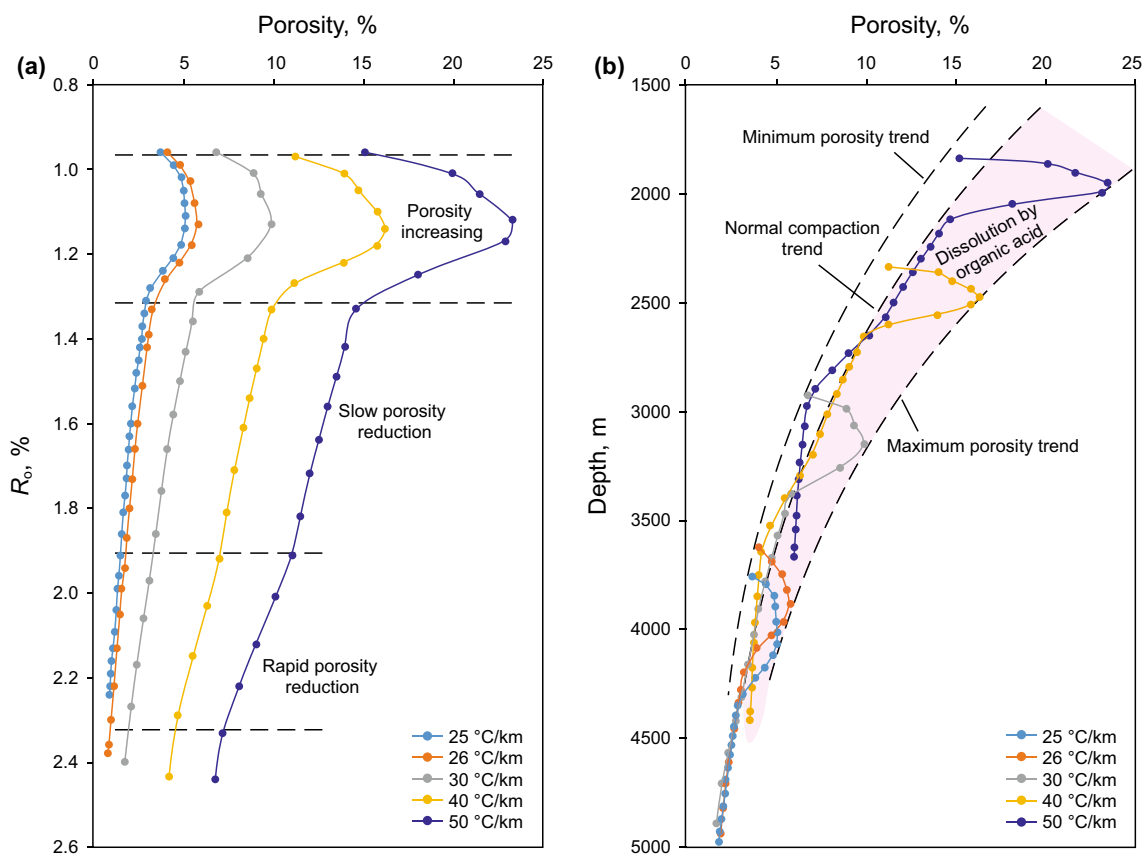


Fig. 10 **a** Relationship between porosity and R_o under different geothermal gradient conditions. **b** Relationship between porosity and depth under different geothermal gradient conditions

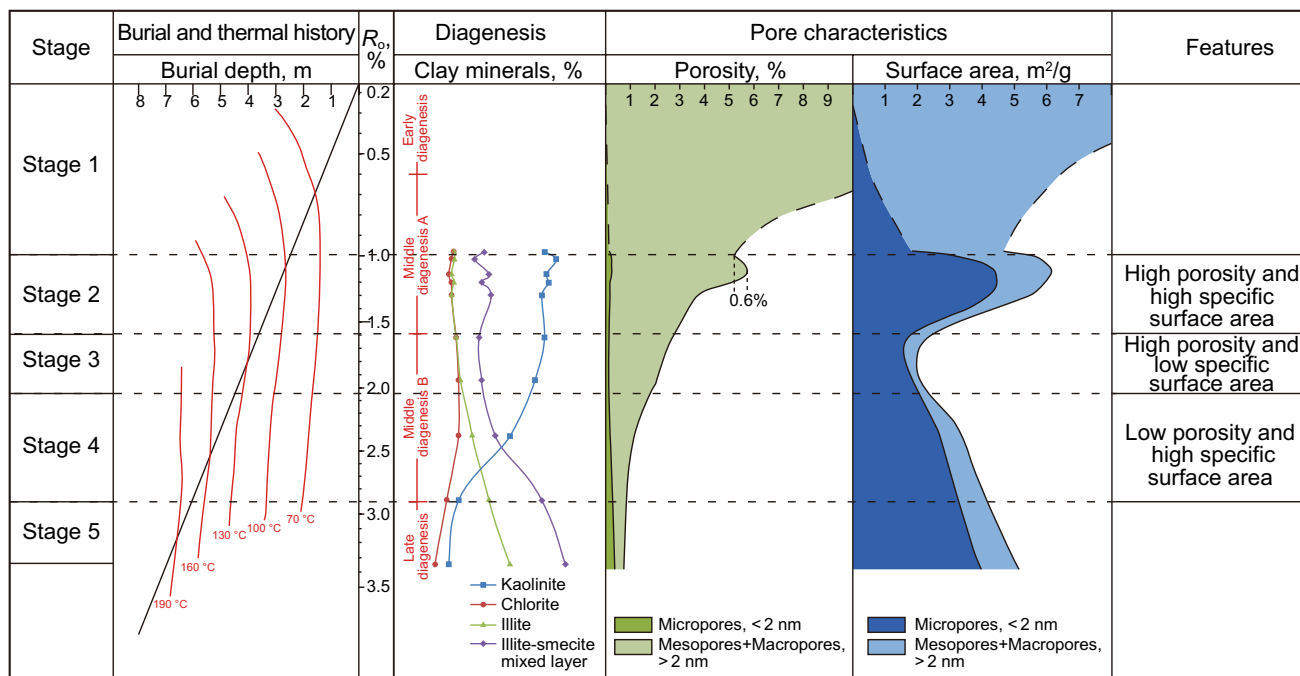


Fig. 11 Pore evolution of the marine-continental transitional shale at simple burial processes and specific geothermal gradients (26 °C/km)

acids. With the dehydration of clay minerals, H^+ and water flow outward (Palomino and Santamarina 2005). Feldspar minerals are dissolved creating a certain amount of dissolved pores which improve the pore connectivity. This process corresponds to the previous stage of porosity increase. The conversion rate of clay minerals is still low, so the most important mechanisms affecting reservoirs at Stage 2 are mechanical compaction and dissolution. In the early period of Stage 2, the volumes of micropores, mesopores and macropores all increased, and the total porosity increased significantly. There is a rapid increase in the specific surface area of micropores. Meanwhile, the specific surface area of mesopores and macropores has stopped decreasing. In the late period of Stage 2, the organic matter is near the peak of oil production, and the liquid hydrocarbons and asphalt will fill the micropores and other pores, which will cause the micropores to be blocked (Löhr et al. 2015). Therefore, the specific surface area of micropores and the total specific surface area rapidly decrease. Stage 2 is characterized by a high porosity and high specific surface area during the pore evolution of marine-continental transitional shale. It is a favorable stage for shale oil and gas exploration.

Stage 3, $1.6\% < R_o \leq 2.0\%$, $120\text{ }^\circ\text{C} < T \leq 140\text{ }^\circ\text{C}$. Kaolinite began to convert to I/S and illite, forming mesopore-sized clay interlayer pores (Wood and Hazra 2017). In addition, the asphalt fillings in the pores have an anti-compaction effect. Both of these reasons cause the porosity to decrease slowly. Therefore, the volume of mesopores and macropores decreased slowly, while the volume of micropores increased. Because the pores are occupied by asphalt and oil, both the specific surface area of micropores and the total specific surface area are the lowest, making it difficult to adsorb gas. Stage 3 is characterized by a high porosity and low specific surface area during the pore evolution of marine-continental transitional shale. It is not an ideal stage for adsorbed gas exploration but may be favorable to explore free gas and light oil.

Stage 4, $2.0\% < R_o \leq 2.9\%$, $140\text{ }^\circ\text{C} < T \leq 175\text{ }^\circ\text{C}$. Kaolinite and chlorite are largely and rapidly converted to I/S and illite. The liquid hydrocarbons formed in the early stage gradually cracked into smaller molecules (Pozo et al. 2017). Gaseous hydrocarbons of small molecules broke through the capillary pressure of the micropores and entered the mesopores and macropores (Modica and Lapierre 2012). The organic matter contracts, creating a large number of organic pores and shrinkage cracks (Chen and Xiao 2014). The asphalt fillings in the pores also mature further and generate many organic pores (Curtis et al. 2012b; Milliken et al. 2013). Therefore, the micropore volume and specific surface area increase significantly. However, this effect also leads to the weakening of the anti-compaction ability of shale, and the loss rate of mesopore and macropore volume increases at high temperature and pressure. Stage 4 is characterized

by a low porosity and high specific surface area during the pore evolution of marine-continental transitional shale. It is a favorable stage for adsorbed gas exploration.

Stage 5, $2.9\% < R_o \leq 3.4\%$, $175\text{ }^\circ\text{C} < T \leq 200\text{ }^\circ\text{C}$. Organic matter reached overmaturity, and clay minerals were in late diagenesis period. The conversion of the clay minerals is about to stop, and the peak of gaseous hydrocarbons in the organic matter has passed. Therefore, the shale pore structure has not changed obviously, but the structure does gradually become denser under higher pressure. The volume and specific surface area of micropores increased slightly, and the volumes of mesopores and macropores decreased continuously. When $R_o > 3.4\%$, organic matter will be carbonized, kerogen aromatization will block the pores, and the pores will collapse under high pressure (Loucks et al. 2012). It is speculated that both pore volume and specific surface area will decrease. Because R_o is beyond the range of thermal simulation experiments, we shall not make a further discussion here.

6 Conclusion

A mechanical compaction model considering clay mineral content and kaolinite proportion was established, and the pore volume results of the thermal simulations were corrected to cause the porosity results to be closer to actual formation conditions. Mechanical compaction models show that shales with higher clay content have a higher initial porosity and faster compaction speed. Cluttered kaolinite is more easily compacted than other clay minerals.

Shales have different pore evolution paths at different geothermal gradients. Geothermal gradients affect thermal evolution and indirectly affect mechanical compaction. Higher geothermal gradients are conducive to preserving higher porosity when the shale matures. The porosity increasing stage of shale with higher geothermal gradients appears at a shallower layer and has a higher increase in porosity.

During the simple burial process at the special geothermal gradient and without considering overpressure, we divided the pore evolution of the marine-continental transitional shale into five stages. Stage 2, in which R_o is 1.0%–1.6%, has a high porosity and high specific surface area; Stage 3, in which R_o is 1.6%–2.0%, has a higher porosity and low specific surface area; and Stage 4, in which R_o is 2.0%–2.9%, has a low porosity and high specific surface area.

Compliance with ethical standards

Conflict of interest The authors declare that we do not have any commercial or associative interest that represents a conflict of interest in connection with the work submitted.

Open Access This article is licensed under a Creative Commons Attribution 4.0 International License, which permits use, sharing, adaptation, distribution and reproduction in any medium or format, as long as you give appropriate credit to the original author(s) and the source, provide a link to the Creative Commons licence, and indicate if changes were made. The images or other third party material in this article are included in the article's Creative Commons licence, unless indicated otherwise in a credit line to the material. If material is not included in the article's Creative Commons licence and your intended use is not permitted by statutory regulation or exceeds the permitted use, you will need to obtain permission directly from the copyright holder. To view a copy of this licence, visit <http://creativecommons.org/licenses/by/4.0/>.

References

- Akande SO, Lewan MD, Egenhoff S, et al. Source rock potential of lignite and interbedded coaly shale of the Ogwashi–Asaba Formation, Anambra basin as determined by sequential hydrous pyrolysis. *Int J Coal Geol.* 2015;150:224–37. <https://doi.org/10.1016/j.coal.2015.09.005>.
- Athy LF. Density porosity and compaction of sedimentary rocks. *AAPG Bull.* 1930;14:1–24. <https://doi.org/10.1306/3D93289E-16B1-11D7-8645000102C1865D>.
- Bachrach R. Mechanical compaction in heterogeneous clastic formations from plastic–poroelastic deformation principles: theory and applications. *Geophys Prospect.* 2017;65:724–35. <https://doi.org/10.1111/1365-2478.12159>.
- Baruch ET, Kennedy MJ, Lohr SC, et al. Feldspar dissolution-enhanced porosity in Paleoproterozoic shale reservoir facies from the Barney Creek Formation (McArthur Basin, Australia). *AAPG Bull.* 2015;99(9):1745–70. <https://doi.org/10.1306/04061514181>.
- Bernard S, Wirth R, Schreiber A, et al. Formation of nanoporous pyrobitumen residues during maturation of the Barnett Shale (Fort Worth Basin). *Int J Coal Geol.* 2012;103:3–11. <https://doi.org/10.1016/j.coal.2012.04.010>.
- Chen J, Xiao XM. Evolution of nanoporosity in organic-rich shales during thermal maturation. *Fuel.* 2014;129:173–81. <https://doi.org/10.1016/j.fuel.2014.03.058>.
- Chen Q, Zhang JC, Tang X, et al. Pore structure characterization of the lower permian marine continental transitional black shale in the Southern North China Basin, Central China. *Energy Fuels.* 2016;30(12):10092–105. <https://doi.org/10.1021/acs.energyfuels.6b01475>.
- Curtis JB. Fractured shale-gas systems. *AAPG Bull.* 2002;86(11):1921–38. <https://doi.org/10.1306/61EEDDBE-173E-11D7-8645000102C1865D>.
- Curtis ME, Cardott BJ, Sondergeld CH, et al. Development of organic porosity in the Woodford Shale with increasing thermal maturity. *Int J Coal Geol.* 2012a;103(103):26–31. <https://doi.org/10.1016/j.coal.2012.08.004>.
- Curtis ME, Sondergeld CH, Ambrose RJ, et al. Microstructural investigation of gas shales in two and three dimensions using nanometer-scale resolution imaging. *AAPG Bull.* 2012b;96(4):665–77. <https://doi.org/10.1306/08151110188>.
- Dong T, Harris NB, Ayranci K, et al. Porosity characteristics of the Devonian Horn River shale, Canada: insights from lithofacies classification and shale composition. *Int J Coal Geol.* 2015;141:74–90. <https://doi.org/10.1016/j.coal.2015.03.001>.
- Gasparik M, Bertier P, Gensterblum Y, et al. Geological controls on the methane storage capacity in organic-rich shales. *Int J Coal Geol.* 2014;123(123):34–51. <https://doi.org/10.1016/j.coal.2013.06.010>.
- Gong F, Di BR, Wei JX, et al. Experimental investigation of mechanical compaction on the physical and elastic properties of synthetic shales. *J Appl Geophys.* 2019;161:139–52. <https://doi.org/10.1016/j.jappgeo.2018.12.011>.
- Guo SB, Mao WJ. Division of diagenesis and pore evolution of a Permian Shanxi shale in the Ordos Basin, China. *J Pet Sci Eng.* 2019;182:106351. <https://doi.org/10.1016/j.petrol.2019.106351>.
- Han YJ, Horsfield B, Wirth R, et al. Oil retention and porosity evolution in organic-rich shales. *AAPG Bull.* 2017;101(6):807–27. <https://doi.org/10.1306/09221616069>.
- Houben ME, Barnhoorn A, Wasch L, et al. Microstructures of Early Jurassic (Toarcian) shales of Northern Europe. *Int J Coal Geol.* 2016;165:76–89. <https://doi.org/10.1016/j.coal.2016.08.003>.
- Jarvie DM, Hill RJ, Ruble TE, et al. Unconventional shale-gas systems: the Mississippian Barnett Shale of north-central Texas as one model for thermogenic shale-gas assessment. *AAPG Bull.* 2007;91(4):475–99. <https://doi.org/10.1306/12190606068>.
- Lan C, Yang B, Peng S. Environment for forming major coal seams of Permian coal-bearing series in Huainan coalfield. *J China Coal Soc.* 1988;3(1):12–22 (in Chinese).
- Liu JS, Ding WL, Wang RY, et al. Quartz types in shale and their effect on geomechanical properties: an example from the lower Cambrian Niutitang Formation in the Cen'gong block, South China. *Appl Clay Sci.* 2018a;163:100–7 (in Chinese).
- Liu KQ, Wang L, Ostadhassan M, et al. Nanopore structure comparison between shale oil and shale gas: examples from the Bakken and Longmaxi Formations. *Pet Sci.* 2018b;16(1):77–93. <https://doi.org/10.1007/s12182-018-0277-3>.
- Löhr SC, Baruch ET, Hall PA, et al. Is organic pore development in gas shales influenced by the primary porosity and structure of thermally immature organic matter? *Org Geochem.* 2015;87:119–32. <https://doi.org/10.1016/j.orggeochem.2015.07.010>.
- Loucks RG, Reed RM, Ruppel SC, et al. Spectrum of pore types and networks in mudrocks and a descriptive classification for matrix-related mudrock pores. *AAPG Bull.* 2012;96(6):1071–98. <https://doi.org/10.1306/08171111061>.
- Luo W, Hou MC, Liu XC, et al. Geological and geochemical characteristics of marine-continental transitional shale from the Upper Permian Longtan formation, Northwestern, Guizhou, China. *Mar Pet Geol.* 2018;89:58–67.
- Ma X, Guo SB. Comparative study on shale characteristics of different sedimentary microfacies of late permian longtan formation in Southwestern Guizhou, China. *Minerals.* 2019;9(1):20. <https://doi.org/10.3390/min9010020>.
- Marcussen O, Thyberg BI, Peltonen C, et al. Physical properties of Cenozoic mudstones from the northern North Sea: impact of clay mineralogy on compaction trends. *AAPG Bull.* 2009;93(1):127–50. <https://doi.org/10.1306/08220808044>.
- Mastalerz M, Schimmelmann A, Drobnick A, et al. Porosity of Devonian and Mississippian New Albany Shale across a maturation gradient: insights from organic petrology, gas adsorption, and mercury intrusion. *AAPG Bull.* 2013;97:1621–43. <https://doi.org/10.1306/04011312194>.
- Metwally YM, Chesnokov EM. Clay mineral transformation as a major source for authigenic quartz in thermo-mature gas shale. *Appl Clay Sci.* 2012;55:138–50. <https://doi.org/10.1016/j.clay.2011.11.007>.
- Milliken KL, Rudnicki M, Awwiller DN, et al. Organic matter-hosted pore system, Marcellus Formation (Devonian), Pennsylvania. *AAPG Bull.* 2013;97(2):177–200. <https://doi.org/10.1306/07231212048>.
- Modica CJ, Lapierre SG. Estimation of kerogen porosity in source rocks as a function of thermal transformation: example from the Mowry Shale in the Powder River Basin of Wyoming. *AAPG Bull.* 2012;96(1):87–108. <https://doi.org/10.1306/04111110201>.
- Palomino AM, Santamarina JC. Fabric map for kaolinite: effects of pH and ionic concentration on behavior. *Clays Clay Miner.*

- 2005;53(3):211–23. <https://doi.org/10.1346/CCMN.2005.0530302>.
- Pozo M, Pino D, Bessieres D. Effect of thermal events on maturation and methane adsorption of Silurian black shales (Checa, Spain). *Appl Clay Sci.* 2017;136:208–18. <https://doi.org/10.1016/j.clay.2016.11.026>.
- Ramadhan AM, Neil RG. Overpressure and mudrock compaction in the Lower Kutai Basin, Indonesia: a radical reappraisal. *AAPG Bull.* 2011;95(10):1725–44. <https://doi.org/10.1306/02221110094>.
- Ross DJK, Bustin RM. The importance of shale composition and pore structure upon gas storage potential of shale gas reservoirs. *Mar Pet Geol.* 2009;26(6):916–27. <https://doi.org/10.1016/j.marpetgeo.2008.06.004>.
- Sun MD, Zhang LH, Hu QH, et al. Pore connectivity and water accessibility in Upper Permian transitional shales, southern China. *Mar Pet Geol.* 2019;107:407–22. <https://doi.org/10.1016/j.marpetgeo.2019.05.035>.
- Teichmüller M. Anwendung kohlenpetrographischer Methoden bei der Erdöl- und Erdgasprospektion. *Erdöl und Kohle* 1971;24:69–76 (in German).
- Tian H, Pan L, Xiao XM, et al. A preliminary study on the pore characterization of Lower Silurian black shales in the Chuandong Thrust Fold Belt, southwestern China using low pressure N₂ adsorption and FE-SEM methods. *Mar Pet Geol.* 2013;48:8–19. <https://doi.org/10.1016/j.marpetgeo.2013.07.008>.
- Valenza JJ, Drenzek N, Marques F, et al. Geochemical controls on shale microstructure. *Geology.* 2013;41(5):611–4. <https://doi.org/10.1130/G33639.1>.
- Wang FT, Guo SB. Influential factors and model of shale pore evolution: a case study of a continental shale from the Ordos Basin. *Mar Pet Geol.* 2019;102:271–82. <https://doi.org/10.1016/j.marpetgeo.2018.12.045>.
- White JM. Compaction of Wyodak Coal, Powder River Basin, Wyoming, USA. *Int J Coal Geol.* 1986;6(2):139–47. [https://doi.org/10.1016/0166-5162\(86\)90017-0](https://doi.org/10.1016/0166-5162(86)90017-0).
- Wood D, Hazra B. Characterization of organic-rich shales for petroleum exploration & exploitation: a review-part 1: bulk properties, multi-scale geometry and gas adsorption. *J Earth Sci.* 2017;28(5):739–57. <https://doi.org/10.1007/s12583-017-0732-x>.
- Xie XM, Amann-Hildenbrand A, Littke R, et al. The influence of partial hydrocarbon saturation on porosity and permeability in a palaeogene lacustrine shale-hosted oil system of the Bohai Bay Basin, Eastern China. *Int J Coal Geol.* 2019;207:26–38. <https://doi.org/10.1016/j.coal.2019.03.010>.
- Xie XM, Volkman JK, Qin JZ, et al. Petrology and hydrocarbon potential of microalgal and macroalgal dominated oil shales from the Eocene Huadian Formation, NE China. *Int J Coal Geol.* 2014;124:36–47. <https://doi.org/10.1016/j.coal.2013.12.013>.
- Yang R, He S, Hu QH, et al. Pore characterization and methane sorption capacity of over-mature organic-rich Wufeng and Longmaxi shales in the southeast Sichuan Basin, China. *Mar Pet Geol.* 2016;77:247–61. <https://doi.org/10.1016/j.marpetgeo.2016.06.001>.
- Yang XG, Guo SB. Pore characterization of marine-continental transitional shale in Permian Shanxi Formation of The Southern North China Basin. *Energy Explor Exploit.* 2020. <https://doi.org/10.1177/0144598720912346>.
- Yin HZ. Acoustic velocity and attenuation of rocks: Isotropy, intrinsic anisotropy and stress induced anisotropy. Ph.D. thesis, Stanford University, USA. 1992.
- Yu K, Ju YW, Qian J, et al. Burial and thermal evolution of coal-bearing strata and its mechanisms in the southern North China Basin since the late Paleozoic. *Int J Coal Geol.* 2018;198:100–15. <https://doi.org/10.1016/j.coal.2018.09.007>.
- Zhang H, Shi JT, Li XF. Optimization of shale gas reservoir evaluation and assessment of shale gas resources in the Oriente Basin in Ecuador. *Pet Sci.* 2018;15(4):756–71. <https://doi.org/10.1007/s12182-018-0273-7>.
- Zou CN, Dong DZ, Wang SJ, et al. Geological characteristics, formation mechanism and resource potential of shale gas in China. *Pet Explor Dev.* 2010;37(6):641–53. [https://doi.org/10.1016/S1876-3804\(11\)60001-3](https://doi.org/10.1016/S1876-3804(11)60001-3).